

Elucidating the roles of chemistry, compositional complexity, and short-range order in the dislocation energetics of body-centered-cubic concentrated solid solutions

Wenqing Wang,^{1,2} Flynn Walsh¹, Robert O. Ritchie^{1,2} and Mark Asta^{1,2,*}

¹Materials Sciences Division, Lawrence Berkeley National Laboratory, Berkeley, California 94720, USA

²Department of Materials Science and Engineering, University of California, Berkeley, California 94720, USA

 (Received 28 August 2023; revised 6 November 2023; accepted 20 December 2023; published 24 January 2024)

Dislocation-mediated deformation mechanisms in body-centered-cubic solid solutions are expected to be influenced by spatial fluctuations in screw dislocation core energies. In refractory high-entropy alloys, the formation of chemical short-range order has been demonstrated to decrease the heterogeneity of this energy landscape, narrowing the distribution of dislocation core energies. It is, however, unclear if multicomponent compositionally complex systems display any unique effects or if these results are more generally applicable. To answer this question, this study computationally investigates how system chemistry, compositional complexity, and the presence of various degrees of chemical short-range order affect the distribution of screw dislocation energies in binary and ternary subsystems of the NbMoTaW alloy. We report the calculated averages and variances for the diffuse antiphase boundary energy and the dislocation core energy with various degrees of chemical short-range order. While short-range order negligibly affects the average core energies, their distributions are notably narrowed in some, but not all, systems, primarily depending on chemistry rather than the number of components.

DOI: [10.1103/PhysRevMaterials.8.013608](https://doi.org/10.1103/PhysRevMaterials.8.013608)

I. INTRODUCTION

Body-centered-cubic (bcc) refractory high-entropy alloys (RHEAs) have attracted extensive interest over the past decade for potential structural materials applications due to their retention of yield strength at elevated temperatures. For high-temperature applications, particular attention has been given to alloys containing Nb, Mo, Ta, and W as principal elements, as originally proposed by Senkov *et al.* [1]. However, the application of many of these materials may be limited by their lack of ductility at ambient conditions [2], in addition to concerns regarding oxidation resistance [3] and high-temperature creep behavior [4,5]. For this reason, the room-temperature damage tolerance of alloys such as NbMoTaW remains as important as their intriguing strength in refractory conditions.

The mechanical properties of bcc metals are traditionally understood to be dictated by the mobility of $\frac{1}{2}\langle 111 \rangle$ screw dislocations [6], although recent work has also highlighted a role of edge dislocations in certain concentrated systems [7,8], especially at elevated temperatures at which the barriers to screw dislocation motion experience significant thermal softening [7]. Deformation at ambient conditions is nonetheless expected to be influenced by screw dislocation glide, which, in pure bcc metals, involves the nucleation [9] and propagation of pairs of kinks in the dislocation line [10–12]. In RHEAs, screw dislocation motion may be particularly inhibited by the large lattice distortion present in a mixture of variously sized elements [13,14].

The mobility of individual screw dislocations is influenced by the spatial distribution of effective core energies, i.e., the Peierls energy landscape, with additional strengthening expected to arise from locking of the dislocations by cross-kink formation [15]. Theoretical Peierls landscapes can be calculated by considering pathways among distinct $\frac{1}{2}\langle 111 \rangle$ screw-core configurations using density functional theory (DFT) or computationally more efficient interatomic potentials. For pure elements, including Nb, Mo, Ta, W, and V, DFT predicts a nondegenerate compact core as the equilibrium structure [16–18], and a Peierls landscape with local minima corresponding to the high-symmetry core structures [19–21]. While the pathways among locally stable core structures provide important information about the shape of the energy landscape [22], their rigorous determination in many-component systems is challenging due to the computational cost of determining transition barriers for even a representative sample of highly variable local chemical environments. It is nonetheless insightful to assess the distribution of minima, or valleys, in the Peierls landscapes of complex alloys. For example, Yin *et al.* [23] predicted a highly heterogeneous distribution of equilibrium $\frac{1}{2}\langle 111 \rangle$ dislocation core DFT energies in NbMoTaW.

Although HEAs are traditionally approximated as solid solutions with random compositional disorder (and hence ideal configurational entropy), a certain amount of local chemical rearrangement will inevitably occur in most systems, as determined by the balance of thermodynamic driving forces and diffusion kinetics. Real refractory alloys will be exposed to a range of elevated temperatures for various amounts of time, with the local ordering of a specific sample likely dependent on its precise thermal history. The kinetics of forming short-range order (SRO) in NbMoTaW alloys are estimated in

*mdasta@berkeley.edu

Sec. IV in light of present and previous [24] thermodynamic calculations.

The presence of SRO contributes to the strengthening of solid solutions in two ways. On one hand, when a dislocation overcomes the Peierls energy barrier and starts to glide, it disturbs any favorable local ordering, creating a diffuse antiphase boundary (DAPB) [25,26]. This DAPB introduces extra energy into the crystal [27], which serves as an athermal strengthening mechanism. On the other hand, SRO alters the stress required for a kink pair to propagate through the solute obstacles, which can be captured by a modified Suzuki model for substitutional solid solution strengthening [28]. In this model, the activation energy for kink propagation is dependent on fluctuations of the local chemical environment, where the prevalence of high-energy regions is reduced by the formation of SRO, and thus softening of the material. The overall effect of SRO is governed by the balance between these two competing mechanisms, which precisely depends on the chemical composition and degree of chemical order [28].

While the effect of local chemical environments on edge dislocation energies is dominated by volumetric interactions that may be efficiently parameterized by misfit volumes [7], for screw dislocations it is generally necessary to consider explicit core-solute interactions [28], which may be at least qualitatively represented by the distribution of Peierls valley energies. In this manner, Yin *et al.* [23] investigated the effects of SRO on NbMoTaW, finding that the presence of SRO can notably decrease the spatial heterogeneity of Peierls minima. It is not clear, however, how these “smoothing” effects depend on the number or type of constituent species in the alloy system. Therefore, the focus of the current paper is to investigate the role of SRO on the dislocation core structures, DAPB energetics, and the core-energy distribution in the ternary and binary subsystems of the NbMoTaW RHEA. The construction of simulation cells for the determination of these systems’ Peierls valley distributions and the calculations of core energies are described in Sec. II and the effects of chemistry, chemical complexity, and short-range order are presented in Secs. III and IV. Our results suggest that SRO decreases the spatial heterogeneity of Peierls valley energies, to a degree that is affected primarily by chemistry rather than the number of alloy components.

II. METHODS

A. Interatomic potential model

To investigate the effects of SRO on the Peierls energy distributions in NbMoTaW and its subsystems, we employ the moment tensor potential (MTP) for NbMoTaW described by Yin *et al.* [15]. This potential, implemented in the Large-scale Atomic/Molecular Massively Parallel Simulator (LAMMPS) [29], was trained using the unary, binary, ternary, and quaternary data of NbMoTaW reported by Li *et al.* [30]. The MTP potential provides near *ab initio* accuracy, while maintaining a reasonable computation cost [31].

B. Estimating order-disorder transition temperatures

To examine the effects of SRO on dislocation energy landscapes, it is important to first establish the equilibrium

ordering temperatures, below which SRO gives way to long-range order. The intent is then to produce states of SRO at various temperatures above the ordering transition temperature T_{tr} . Hence we perform simulations to estimate T_{tr} from simulated heat-capacity calculations, as described below. To estimate the order-disorder transition temperature of each subsystem, we calculated the configurational contribution to the heat capacity (C_V) at various temperatures using on-lattice canonical Monte-Carlo (MC) sampling (Fig. S4 in the Supplemental Material [32]).

It has been shown that lattice relaxation significantly alters the order-disorder transition temperature of NbMoTaW [24,33], but has limited effects on the ordering at temperatures above the order-disorder transition [24]. To assess the potential effects from atomic displacements (lattice distortions) and thermal expansion on the state of SRO, we conducted additional hybrid Molecular-Dynamics/Monte-Carlo (MD/MC) simulations for each of the systems at a temperature of $1.1 \times T_{tr}$ (where T_{tr} is derived from the on-lattice simulations). The magnitudes of the Warren-Cowley (WC) parameters obtained from the hybrid MD/MC simulations were found to differ from those derived in the on-lattice MC simulations by less than 10% (Fig. S6 in the Supplemental Material [32]). Additionally, the signs of these parameters for the different bond types were in agreement for the two types of simulations. Thus, we employ on-lattice MC simulations to generate representative states of SRO for the current studies.

On-lattice MC simulations were performed with supercells that are $5 \times 5 \times 5$ repetitions of the conventional bcc unit cell containing 250 atoms for each composition. The equilibrium lattice constants were determined for orthogonal supercells with random compositional arrangements for each subsystem employing zero-temperature energy relaxation calculations in which the shape and dimension of the simulation cell is optimized under zero external pressure. From the equilibrium dimension and shape of the resulting relaxed structure, the lattice constant was calculated as $a_0 = (2v_0)^{1/3}$, where v_0 is the equilibrium atomic volume. The calculated equilibrium lattice constants so obtained are as follows: NbMoTaW 3.2376 Å, NbMoTa 3.2634 Å, NbMoW 3.2159 Å, MoTaW 3.2128 Å, NbMo 3.2361 Å, MoTa 3.2323 Å, and TaW 3.2384 Å.

On-lattice MC simulations were used to equilibrate the systems and calculate heat capacities at temperatures between 2000 and 350 K. In these MC simulations, the cell shape was constrained to remain cubic with the volume fixed at values corresponding to the lattice constants given above. Attempted swaps of two atoms of different types, sampled randomly, were accepted or rejected based on the Metropolis algorithm. At each temperature, the total length of the simulation was 2000 MC passes, where a pass consists of N attempted swaps, with N the number of atoms. Simulations were performed initially at 2000 K starting from a random bcc configuration, and subsequently at a consecutive set of lower temperatures reduced in 50 K intervals; the ending configuration of the prior simulation was used to seed the next at each subsequent lower temperature.

At all temperatures, the total energy of every subsystem was judged to be equilibrated after 500 MC passes. After 500 MC passes, the heat capacity (C_V) was calculated from the energy (E) fluctuations: $C_V = [\langle E^2 \rangle - \langle E \rangle^2] / k_B T^2$. The

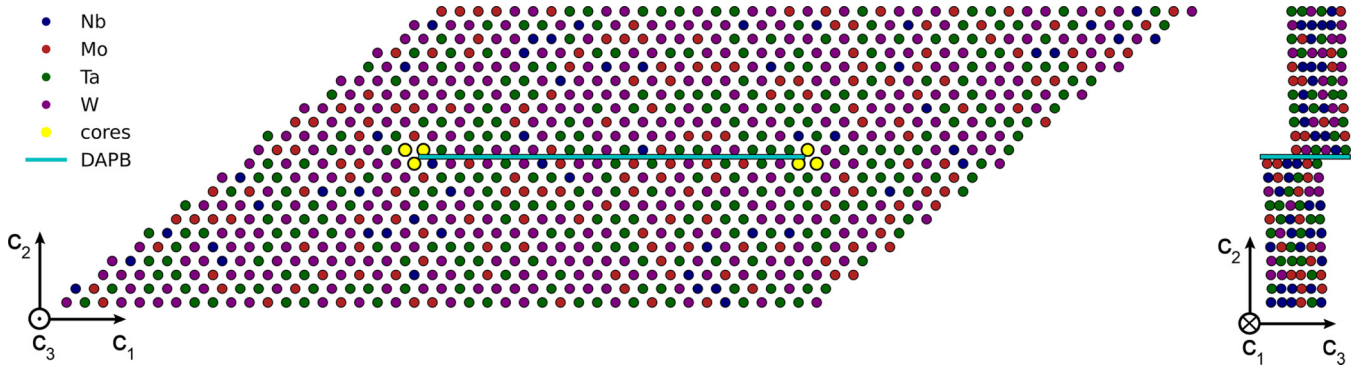


FIG. 1. Supercell setup with a dislocation dipole, where the DAPB is marked by the light-blue line and the dislocation cores with opposite Burgers vectors are highlighted with yellow circles. The left panel is viewed along the C_3 direction (corresponding to the dislocation line direction), and the right panel is viewed from the perpendicular C_1 direction, where $C_1 = [\bar{1}\bar{1}2]$, $C_2 = [1\bar{1}0]$, and $C_3 = [111]$. The supercell is repeated along the C_3 direction once, giving a thickness of two Burgers vectors. This thickness is given for all systems considered in the text. The example shown in this figure is for the NbMoTaW quaternary system containing only 1848 atoms for better illustration, and the chemical species are indicated by the different colors. The supercell where the statistical analysis is made in this paper contains 7392 atoms.

value of T_{tr} was then identified from peaks in C_V versus temperature (Fig. S4 in the Supplemental Material [32]). Neglecting atomic relaxations and vibrations, seven systems were found to undergo an order-disorder transition above 500 K: NbMoTaW 850 K, NbMoTa 950 K, NbMoW 550 K, MoTaW 900 K, NbMo 1050 K, MoTa 1750 K, TaW 800 K. SRO was considered to be minimally relevant in other systems, which were not examined further.

C. Dislocation relaxation

To investigate the spatial distribution of screw dislocation core energies, a simulation cell was constructed to contain a dislocation dipole, as illustrated in Fig. 1. In this setup, a quadrupolar cell arrangement [35,36] was used to maximize the distances between the dislocations and its periodic images, while minimizing image stress. The simulation supercell contained 7392 atoms and was oriented with the periodic directions along the vectors of $C_1 = a_0[\bar{1}\bar{1}2]$, $C_2 = a_0[1\bar{1}0]$, and $C_3 = a_0[111]$, where a_0 is the equilibrium lattice constant determined for each subsystem. The periodic length of the C_3 dislocation line direction is two Burgers vectors. This value is fixed for all systems considered in the text, and it is important to note that the distributions and their variances specifically hold for this value of the dislocation line length. Five representative states of SRO were then derived for each composition, from on-lattice MC simulations at temperatures of $1.1 T_{tr}$, $1.4 T_{tr}$, $1.7 T_{tr}$, $2.0 T_{tr}$, and $2.3 T_{tr}$. For each temperature, the SRO was derived from the final state resulting from a MC simulation with 500 passes. With this procedure, the state resulting from the simulation at $1.1 T_{tr}$ corresponds to the maximum level of SRO, those at $2.3 T_{tr}$ the least, and those from the temperatures in between giving intermediate degrees of local order.

For each dislocation supercell, the positions of the atoms were initialized using displacements from anisotropic elasticity theory for the dipole configuration, using the BABELcode [37]. The atomic positions were subsequently relaxed using a conjugate-gradient algorithm in LAMMPS until the energy difference between two successive iterations divided by the

magnitude of total energy is less than 1×10^{-9} , which approximately corresponds to an energy convergence criteria of 1.2×10^{-5} eV/atom.

The above procedure was repeated for a random configuration, and five configurations with SRO, for each composition. The SRO configurations were derived from MC simulations using the approach and temperatures based on the values of T_{tr} listed in the previous section. To gather a statistical distribution of dislocation core energies, the dislocation dipole was initialized at each independent Peierls valley position for each of the configurations. Figure 2 shows representative relaxed dislocation core structures in the (a) random, (b) $1.4 T_{tr}$, and (c) $1.1 T_{tr}$ configurations of NbMoTa. Similar dislocation core structures are also observed in other systems, indicating that the nondegenerate compact core remained the equilibrium structure for the configurations that were examined, irrespective of the composition or degree of SRO.

To compute core energies for each relaxed supercell, we followed the procedure described by Yin *et al.* [23]. Specifically, we computed the excess energy as the difference between the relaxed energy for a given configuration with and without the dislocation dipole. From this excess energy (E_{excess}), the core energy (E_{core}) is derived from the following formula:

$$E_{excess} = E_{core} + E_{elas} + E_{DAPB}, \quad (1)$$

where E_{elas} is the elastic energy contribution and E_{DAPB} is the DAPB energy in configurations with SRO.

The elastic energy is calculated using the method described in Ref. [37], as implemented in the BABEL code. In computing these quantities, we assumed that they varied negligibly with SRO. We computed their values for systems with local order at each composition for a configuration corresponding to the equilibrium state of SRO at $1.1 T_{tr}$. The values of the elastic constants required to compute elastic energies were calculated for each refractory subsystem with random and SRO configurations using LAMMPS and the MTP potential. For each configuration, uniaxial (ϵ_{xx} , ϵ_{yy} , ϵ_{zz}) and simple shear (ϵ_{xy} , ϵ_{xz} , ϵ_{yz}), deformation were applied with a strain $\epsilon = 1 \times 10^{-6}$,

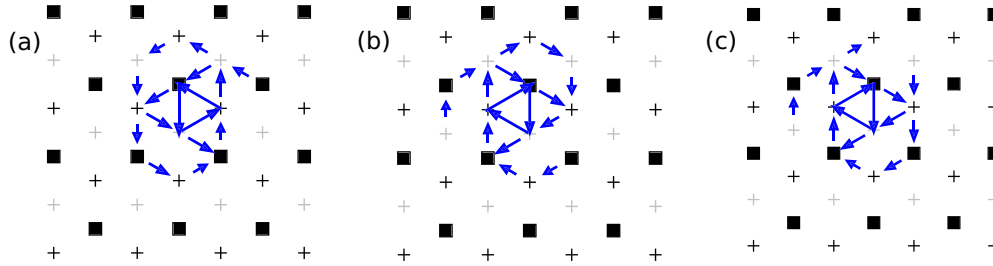


FIG. 2. The differential displacement map [34], viewed along the dislocation line (i.e., [111]) direction, for the relaxed dislocation core structures in the (a) random, (b) $1.4 T_{tr}$, and (c) $1.1 T_{tr}$ configurations of NbMoTa. The black squares, and the black and gray plus signs, represent the different stacking layers along the [111] direction. Note that only the displacements that are larger than $0.1 \times \frac{1}{2}(111)$ are shown.

followed by atomic relaxation with the same minimization criteria as described in the paragraphs above. From the calculated stresses for each simulation cell, the corresponding elastic moduli are derived. Since the method in Ref. [37] requires elastic constants of the single-crystal elastic constants with cubic symmetry, we further reduced the calculated elastic modulus tensor into three cubically symmetrized values (\tilde{C}_{11} , \tilde{C}_{22} , and \tilde{C}_{33}),

$$\begin{aligned}\tilde{C}_{11} &= \frac{C_{11} + C_{22} + C_{33}}{3}, \\ \tilde{C}_{12} &= \frac{C_{12} + C_{13} + C_{23}}{3}, \\ \tilde{C}_{44} &= \frac{C_{44} + C_{55} + C_{66}}{3},\end{aligned}$$

where the C_{ij} denote elastic constant values in a given random or SRO configuration. The symmetrized elastic constants are also used to generate the initial displacement fields for inserting the dislocation dipole into the supercell.

The DAPB energy results from the ‘‘cut’’ plane between the dislocation cores, which results in a relative displacement of the lattice planes by a Burgers vector, thus disrupting the SRO (see Fig. 1). The DAPB energy was computed following the approach described by Yin *et al.* [23], as illustrated in Fig. S1 in the Supplemental Material [32]. In this approach, one layer of atoms with the same length as the planar cut is shifted by one Burgers vector in a configuration without a dislocation dipole (Fig. S1 in the Supplemental Material [32]). From half the difference between the relaxed energy of this configuration, and the corresponding reference bulk configuration, the value of the DAPB energy (E_{DAPB}) is derived (the factor of a half accounts for the two DAPBs created by the procedure). This calculation of E_{DAPB} was performed at every possible atomic layer to maximize statistical sampling.

To quantify the effect of SRO on the roughness of the Peierls energy landscape, we report values for the variance (σ_{core}^2) of the core energy. To compute this value for a given configuration, it is necessary to separate the variance of excess energy into the variances from its contributing factors. By assumption, the elastic energy is constant in a given atomic configuration and hence does not contribute to the variance (σ_{excess}^2) of the excess energy. Assuming that the core energy and DAPB energy are uncorrelated, their contributions to the

variance of the excess energy are additive,

$$\sigma_{excess}^2 = \sigma_{core}^2 + \sigma_{DAPB}^2, \quad (2)$$

where σ_{DAPB}^2 is the variance of the DAPB energy. In what follows, we will examine how the dislocation core-energy distribution is affected by the equilibrium ordering, and chemical composition.

III. RESULTS

A. Short-range order parameters

The SRO derived from the on-lattice MC simulations described in Sec. II B is plotted in Fig. 3 considering first- and second-nearest-neighbor Warren-Cowley (WC) SRO parameters [38,39]. For a pair of types i and j , the WC parameter is defined as

$$\alpha_{ij} = 1 - P(j|i)/c_j, \quad (3)$$

where the $P(j|i)$ is the probability of finding the species j as a neighbor to a site occupied by species i , and c_j is the relative concentration (mole fraction) of species j . A negative WC parameter indicates an enhancement of bonds of type $i - j$ in the neighbor shell relative to the random state, while a positive value indicates a reduction in pairs of this type.

The WC parameters plotted in Fig. 3 are significant in magnitude and display values consistent with tendencies to form long-range-ordered phases. Within the nearest-neighbor shell, the most dominantly preferred bonding pairs are Mo-Ta (in NbMoTaW, NbMoTa, MoTaW, and MoTa), Mo-Nb (in NbMoTaW, NbMoW, and NbMo), and Ta-W (in NbMoTaW and TaW), while the main unfavorable pairs are Mo-Mo (in every Mo-containing system), Ta-Ta (in every Ta-containing system), and Nb-Ta (in NbMoTaW and NbMoTa). The qualitative trends in the SRO are preserved up to $2.3 T_{tr}$ (Fig. 3). At 300 K, the equilibrium configurations of the binaries (NbMo, MoTa, and TaW) and the NbMoTaW system are consistent with an ordered B2 structure, where in the quaternary alloy, Mo and W occupy one sublattice while Nb and Ta occupy the other. Though the ordering structure for the ternary alloys is less obvious, the general bonding preferences, including B2 phase formation in the binaries and the NbMoTaW system, qualitatively agree with previous studies [23,24,40–42].

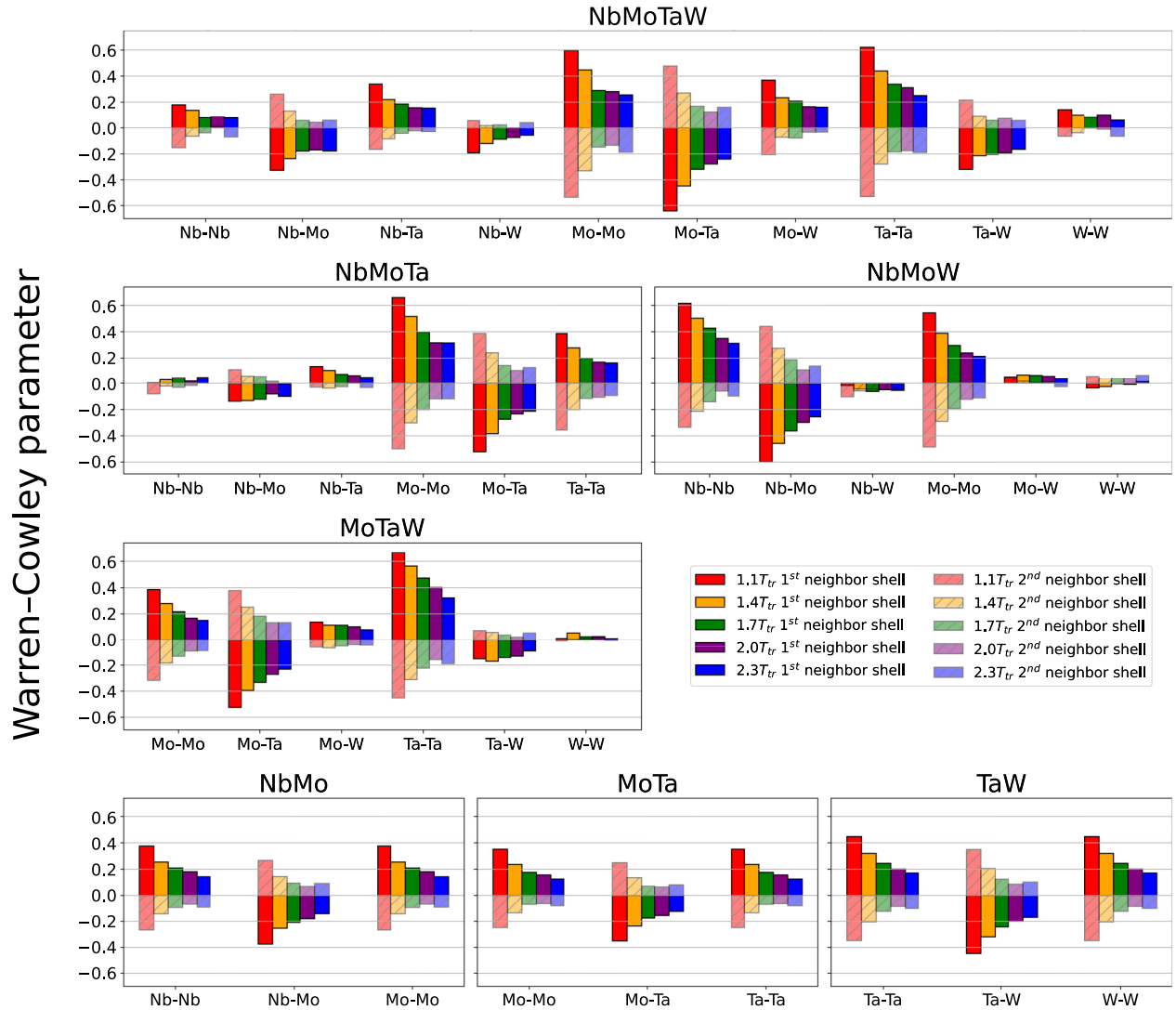


FIG. 3. First- (solid) and second- (hatched) nearest-neighbor Warren-Cowley SRO parameters for each atom pair in NbMoTaW and its ternary and (some) binary subsystems. For each panel, and each pair type, the values from left to right correspond to temperatures of $1.1 T_{tr}$, $1.4 T_{tr}$, $1.7 T_{tr}$, $2.0 T_{tr}$, and $2.3 T_{tr}$, where the values of T_{tr} for each system can be found in Sec. II.

B. Average dislocation core and DAPB energy

Figure 4 plots the distributions of the excess energies of the dislocation dipole supercells for each composition, and each of the six states of SRO: random, $1.1 T_{tr}$, $1.4 T_{tr}$, $1.7 T_{tr}$, $2.0 T_{tr}$, and $2.3 T_{tr}$. The histograms of the calculated excess energies are each well fit by a Gaussian distribution and can be characterized by the mean and variance (σ_{excess}^2). Both of these quantities vary based on the composition and state of the SRO. To justify the assumption of Gaussian distributions, we have analyzed higher-order moments, namely, the third- and fourth-order moments defined through the skewness and kurtosis, respectively. As shown in the Supplemental Material [32], these analyses support the assumption that the excess energies are well modeled by Gaussian distributions.

We consider next the average values of the core and DAPB energies derived from these E_{excess} distributions. Their contributions to the average excess energies are plotted in Fig. 5, where it should be emphasized that the core energies are averaged over the two dislocations in the supercell. For the

average core energies for the NbMoTaW system, the values derived in this study with the MTP potential agree to within 10% of the values derived in the *ab initio* studies by Yin *et al.* [23]. This level of discrepancy likely arises due to the differences between the descriptions of the potential energy used here versus the DFT results, and/or the larger system size used in the present study. It is important to note that the values of the core energies presented in this manuscript depend on the choice of core radius (r_{core}) used in the calculations of the elastic energy. The value chosen was the default value used in BABEL, namely, $r_{\text{core}} = a_0$, where a_0 is the lattice constant. If this value is changed, the elastic energy will change accordingly, as well as the mean values of the core energy for each system. For example, a change from $r_{\text{core}} = a_0$ to $r_{\text{core}} = 1.3a_0$ leads to an increase in the core energy by approximately 14–25% for the different systems considered in our study. Importantly, however, the elastic energy, by definition, does not vary with the position of the dislocations within the supercells, so that changes in this quantity will not influence

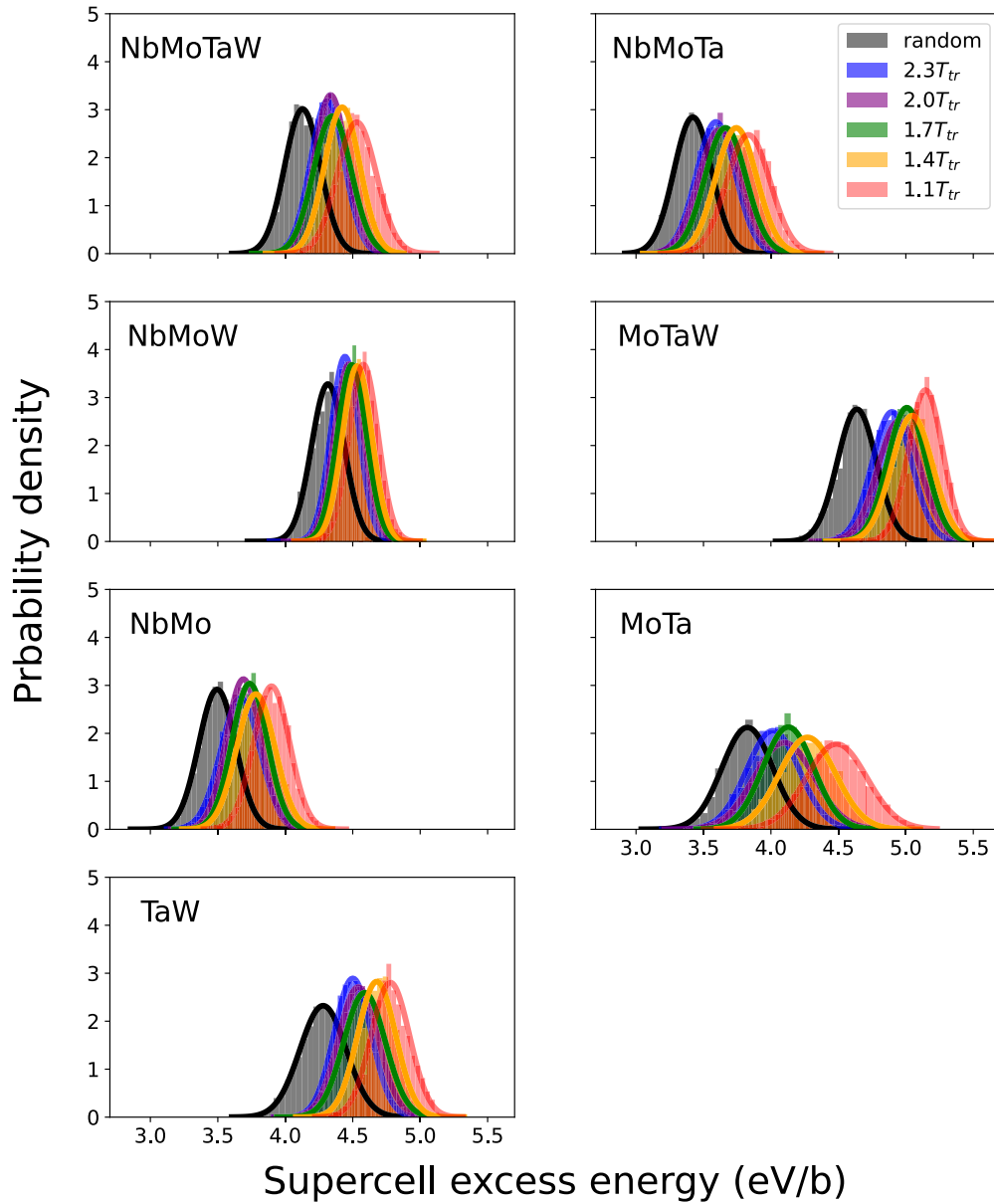


FIG. 4. The supercell excess energy distributions for the NbMoTaW and its subsystems. In each panel, the bars indicate the calculated histogram data and the solid lines indicate Gaussian fits. For each panel, results are plotted for random configurations (gray bars and solid black lines) and configurations with different levels of SRO as indicated in the legend according to the equilibration temperatures, where the values of T_{tr} for each system can be found in Sec. II.

the calculated variances of the core energy and conclusions concerning the effect of SRO upon them.

The average core energies are plotted in Fig. 5 and listed in Table I. These values are found to display larger variations with composition than with the state of the SRO. Specifically, for each of the subsystems that is considered, the largest difference between the core energies for the random configuration and the state with the largest degree of SRO (i.e., at $1.1T_{tr}$) is 9% (0.1 eV/b) for MoTa, with the state with the SRO having lower core energy. This trend of smaller core energy for the state with the largest degree of SRO compared to the random configuration holds for all of the systems that are considered, although the magnitude of the change is smaller for all of the other systems. By contrast, the variation of average

core energy with composition is larger, as can be seen from a comparison of the values for the random configurations, which span a range of approximately 0.3 eV/b (about 20% of the maximum value). An interesting feature of the calculated results for core energies is that there is no clear trend with the number of components. The largest core energies are found in the systems containing W atoms.

The contribution of the DAPBs to the average excess energies is plotted in Fig. 5, and in Table II the average values of E_{DAPB} are listed in the natural units of energy per unit area. For all of the random systems that are considered, the average value of E_{DAPB} is zero within statistical sampling errors, and the magnitudes increase with increasing degree of SRO (i.e., decreasing temperature), as is apparent from Table II. As

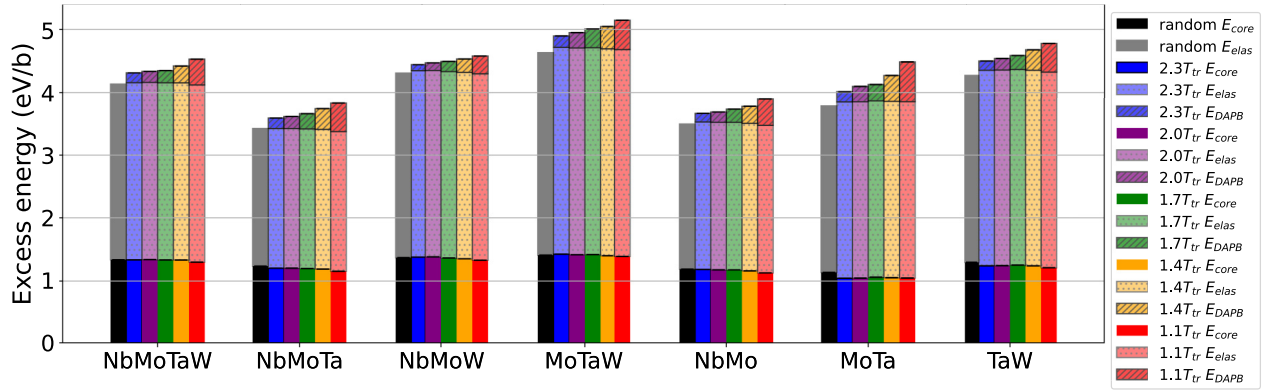


FIG. 5. The average supercell excess energy decomposed into contributions (from bottom to top) corresponding to the core energy (E_{core}), the elastic energy (E_{elas}), and the DAPB energy (E_{DAPB}). For each system, the results are plotted for random configurations (black and gray) and configurations with varying degrees of SRO as indicated in the legend according to the different equilibration temperatures (the values of T_{tr} for each system can be found in Sec. II). The average DAPB energy for the random cells is zero, and thus is not shown in this figure.

with the average core energies, there is no clear trend in the magnitudes of E_{DAPB} with number of components. The largest values at $1.1 T_{\text{tr}}$ are calculated for the MoTa binary, and the NbMoTa and MoTaW ternaries, where the values are over 90 mJ/m^2 .

C. Dislocation core-energy distribution

We consider next the effect of SRO on the distribution of core energies, i.e., the extent to which local ordering flattens the landscape of Peierls valley energies. Figure 6 decomposes variances of the excess energies into the contributions from core energies and DAPBs, for each composition and level of SRO. Note that the nonzero variance for the DAPB distribution for random cells is due to the finite size of the sampled DAPB area, which was chosen to correspond to that present in the dislocation supercells. Before discussing these results, and the implication of SRO effects, it is important to emphasize that the values plotted in Fig. 6 are obtained from a single supercell. Therefore, it is necessary to determine the degree to which these results are converged with respect to sampling statistics.

To check the statistical uncertainties associated with these results, we considered the four-component NbMoTaW system and investigated the random sample and the system with the highest degree of SRO ($1.1 T_{\text{tr}}$). For each of these two systems,

we generated 10 configurations and computed the distribution of core energies. The error bars in Fig. 6 are centered on the average values and reflect the standard deviation in the variances of the 10 configurations. Assuming normal distribution of the dislocation core variance, two 90% confidence intervals, for random and $1.1 T_{\text{tr}}$ SRO configurations, were constructed based on the above sampling. The random and the $1.1 T_{\text{tr}}$ SRO confidence zones do not overlap, indicating that the variances in the random and the $1.1 T_{\text{tr}}$ SRO configurations are statistically different. For the other systems considered in this work, we will assume that the statistical sampling errors derived for the NbMoTaW system are representative across the different compositions and states of the SRO.

Based on the above assumptions, we interpret the results presented in Fig. 6. For NbMoW and TaW, we find statistically significant differences in the core-energy variances between the random configuration and all of the samples with SRO (i.e., for all samples equilibrated at T below $2.3 T_{\text{tr}}$). By contrast, the changes in core-energy variances with SRO for NbMoTa and MoTa are sufficiently small that they cannot be discerned with the level of sampling employed in this work. For NbMoTaW, NbMo, and MoTaW, statistically significant differences in the core-energy variances are found relative to the random configuration, only for those systems where the degree of SRO is sufficiently large (i.e., for T/T_{tr} less

TABLE I. Average dislocation core energy for different compositions and levels of SRO. The first column lists the system composition, and the second through seventh columns list the values of the core energies (in units of eV/b) for different levels of SRO.

	$1.1 T_{\text{tr}}$	$1.4 T_{\text{tr}}$	$1.7 T_{\text{tr}}$	$2.0 T_{\text{tr}}$	$2.3 T_{\text{tr}}$	Random
NbMoTaW	1.3	1.3	1.3	1.3	1.3	1.3
NbMoTa	1.2	1.2	1.2	1.2	1.2	1.2
NbMoW	1.3	1.4	1.4	1.4	1.4	1.4
MoTaW	1.4	1.4	1.4	1.4	1.4	1.4
NbMo	1.1	1.2	1.2	1.2	1.2	1.2
MoTa	1.0	1.1	1.1	1.0	1.0	1.1
TaW	1.2	1.2	1.3	1.2	1.2	1.3

TABLE II. Average DAPB energy (mJ/m^2) for different compositions and levels of SRO. The average values of E_{DAPB} for the random simulation cells are zero within statistical sampling errors and thus are not shown in this table.

	$1.1 T_{\text{tr}}$	$1.4 T_{\text{tr}}$	$1.7 T_{\text{tr}}$	$2.0 T_{\text{tr}}$	$2.3 T_{\text{tr}}$
NbMoTaW	84	55	40	36	32
NbMoTa	93	68	50	39	34
NbMoW	59	44	34	25	20
MoTaW	97	74	62	51	38
NbMo	87	57	44	34	28
MoTa	130	85	54	51	34
TaW	94	67	46	38	30

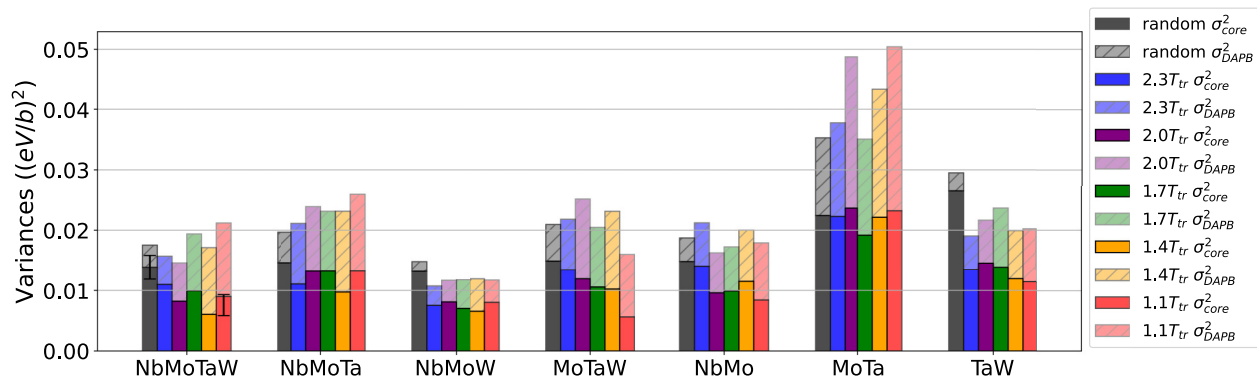


FIG. 6. The effect of SRO on the variances of core-energy distributions in subsystems of NbMoTaW. The solid and hatched bars indicate contributions to the variances of excess energies arising from core energies and DAPB energies, respectively. The average DAPB energy for the random cells is zero, and the nonzero variance for the DAPB distribution for random cells is due to the finite size of the sampled DAPB area. For each system, the results are plotted for random configurations (black and gray) and configurations with varying degrees of SRO as indicated in the legend according to the different equilibration temperatures (the values of T_{tr} for each system can be found in Sec. II). The error bars plotted for NbMoTaW represent estimated uncertainties in the variances of core energies, estimated in the manner described in Sec. III C.

than approximately 2.0 for the first two compositions, and approximately 1.7 for the third).

IV. DISCUSSION

Overall, the results in the current work suggest that the effects of SRO on the variance of the distribution of core energies can be large (over 50% for MoTaW and TaW). However, the degree of narrowing of core energies shows no clear trend with composition or number of components.

Given the potentially significant effects of SRO on core-energy distributions in the refractory concentrated alloys investigated here, it is interesting to consider the conditions under which this local order may form kinetically. For this purpose, we estimate SRO relaxation times, i.e., the time for SRO to form from an initially random configuration, using concentration-wave kinetics theory [43]. A recent comparison between this mean-field theory and kinetic Monte Carlo simulations for model binary alloys demonstrated agreement at the level of an order of magnitude [46]. For the present system, we consider binary alloys and employ formulas presented by Cook [43], who provides a simple method for assessing the isothermal equilibration time of binary regular solutions based on experimental interdiffusion measurements.

The theoretical diffusivity of NbMoTaW lies below that of Nb and Ta, but well above that of Mo or W [47]. Thus, the behavior of this class of alloys may be roughly gauged by considering interdiffusion in the two distinct binary systems for which experimental data are readily available, specifically, NbMo [44] and TaW [45]. While none of these systems can be realistically considered regular solutions [48], the approximation is nonetheless employed with some frequency [49,50] and is assumed to be adequate for the purposes of these estimates.

The resulting expression for the relaxation time (τ) is

$$\tau = \frac{a^2}{32\tilde{D}} \frac{T + T_c}{T - T_c}, \quad (4)$$

where \tilde{D} is the interdiffusion coefficient and T_c is the critical temperature of ordering [43], which we approximate here

as the value of T_{tr} derived from the on-lattice Monte Carlo simulations presented above.

Figure 7 plots the resulting values of τ for binary NbMo and TaW alloys. If the values are also representative for related HEA compositions, they suggest that typically employed thermal histories realized in the processing of these materials may lead to the formation of SRO. Specifically, in Ref. [51], NbMoTaW and NbMoTaWV alloys were annealed at 1673 K (approximately $2 T_c$) for 19 hours (68 400 s), and in Ref. [52], NbMoTaW samples were annealed at 2073 K (approximately $2.44 T_c$) for seven days (604 800 s). For both systems, these annealing times are significantly longer than the relaxation times plotted at the respective temperatures in Fig. 7, suggesting that they may be sufficient to enable SRO to form kinetically.

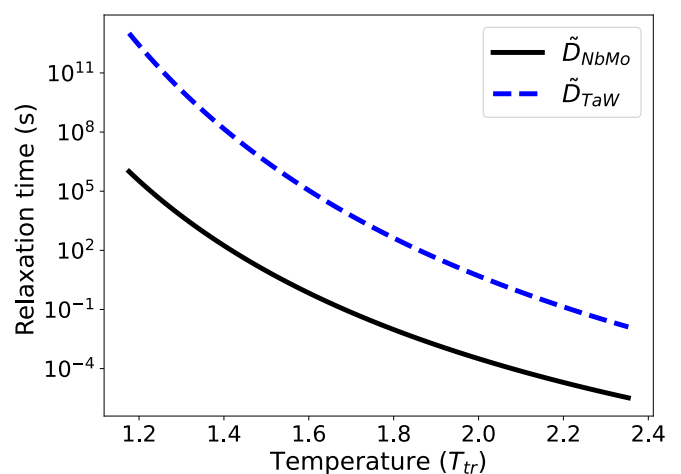


FIG. 7. The relaxation time, which approximates the time required for the equilibration of SRO, calculated using the expressions from Cook [43], based on mean-field concentration-wave theory. Results are plotted assuming a representative ordering temperature of 850 K, and the interdiffusion coefficients measured for NbMo [44] and TaW [45].

V. CONCLUSION

We present an analysis of the effects of chemical SRO on $\frac{1}{2}\langle 111 \rangle$ screw dislocation core-energy distributions in bcc RHEA NbMoTaW and its equimolar ternary and binary subsystems. In each of the systems that is considered, chemical SRO equilibrated at temperatures lower than $2.3 T_{tr}$ does not significantly change the average value of the core energy, but its presence decreases the variance of the core energy significantly in some, but not all, of these systems. Whether SRO “narrows” the Peierls energy distribution depends on both the chemistry and the equilibration temperature, rather than being determined exclusively by the number of components. In other words, the magnitude of the effect of SRO on the variance of dislocation core energies depends on the chemistry of the system, rather than being simply dictated by high configurational entropy. Based on the estimation of ordering kinetics, certain experimental homoge-

nization and operating conditions could enable the formation of appreciable SRO, such that the results presented here become relevant for modeling of mechanical behavior in these systems.

ACKNOWLEDGMENTS

This work was supported by the U.S. Department of Energy, Office of Science, Office of Basic Energy Sciences, Materials Sciences and Engineering Division, under Contract No. DE-AC02-05-CH11231 within the Damage Tolerance in Structural Materials (KC 13) program.

The study made use of resources of the National Energy Research Scientific Computing Center (NERSC), a U.S. Department of Energy Office of Science User Facility located at Lawrence Berkeley National Laboratory, operated under the same contract number, using NERSC Award No. BES-ERCAP0027535.

-
- [1] O. Senkov, G. Wilks, D. Miracle, C. Chuang, and P. Liaw, *Intermetallics* **18**, 1758 (2010).
- [2] Z. Han, H. Luan, X. Liu, N. Chen, X. Li, Y. Shao, and K. Yao, *Mater. Sci. Engineer. A* **712**, 380 (2018).
- [3] L. Shao, Z. Liu, and Y. Zou, *J. Alloys Compd.* **927**, 166946 (2022).
- [4] P. Kral, W. Blum, J. Dvorak, N. Yurchenko, N. Stepanov, S. Zherebtsov, L. Kuncicka, M. Kvapilova, and V. Sklenicka, *Mater. Sci. Engineer. A* **783**, 139291 (2020).
- [5] X. Shen, S. Xin, S. Ding, Y. He, W. Dong, B. Sun, X. Cai, T. Shen *et al.*, *J. Mater. Res. Technol.* **24**, 4796 (2023).
- [6] F. Maresca and W. A. Curtin, *Acta Mater.* **182**, 144 (2020).
- [7] F. Maresca and W. A. Curtin, *Acta Mater.* **182**, 235 (2020).
- [8] Q. He, S. Yoshida, and N. Tsuji, *Scr. Mater.* **231**, 115442 (2023).
- [9] H. Koizumi, H. Kirchner, and T. Suzuki, *Acta Metall. Mater.* **41**, 3483 (1993).
- [10] H. Suzuki, Solid-solution hardening in body-centered cubic alloys, in *Dislocations in Solids*, edited by F. R. N. Nabarro (North Holland, Amsterdam, 1979), p. 191.
- [11] W. Spitzig, *Acta Metall.* **18**, 1275 (1970).
- [12] D. Caillard and J.-L. Martin, *Thermally Activated Mechanisms in Crystal Plasticity* (Elsevier, Amsterdam, 2003).
- [13] I. Toda-Caraballo, J. Wróbel, S. Dudarev, D. Nguyen-Manh, and P. Rivera-Díaz-del Castillo, *Acta Mater.* **97**, 156 (2015).
- [14] R. Kozak, A. Sologubenko, and W. Steurer, *Z. Kristallogr. Crystal. Mater.* **230**, 55 (2015).
- [15] S. Yin, Y. Zuo, A. Abu-Odeh, H. Zheng, X.-G. Li, J. Ding, S. P. Ong, M. Asta, and R. O. Ritchie, *Nat. Commun.* **12**, 4873 (2021).
- [16] C. Woodward and S. Rao, *Philos. Mag. A* **81**, 1305 (2001).
- [17] S. L. Frederiksen and K. W. Jacobsen, *Philos. Mag.* **83**, 365 (2003).
- [18] C. R. Weinberger, G. J. Tucker, and S. M. Foiles, *Phys. Rev. B* **87**, 054114 (2013).
- [19] K. Ito and V. Vitek, *Philos. Mag. A* **81**, 1387 (2001).
- [20] C. R. Weinberger, B. L. Boyce, and C. C. Battaile, *Intl. Mater. Rev.* **58**, 296 (2013).
- [21] M. Mrovec, D. Nguyen-Manh, D. G. Pettifor, and V. Vitek, *Phys. Rev. B* **69**, 094115 (2004).
- [22] L. Dezerald, L. Ventelon, E. Clouet, C. Denoual, D. Rodney, and F. Willaime, *Phys. Rev. B* **89**, 024104 (2014).
- [23] S. Yin, J. Ding, M. Asta, and R. O. Ritchie, *npj Comput. Mater.* **6**, 110 (2020).
- [24] T. Kostiuchenko, F. Körmann, J. Neugebauer, and A. Shapeev, *npj Comput. Mater.* **5**, 55 (2019).
- [25] M. Zhang, Q. Yu, C. Frey, F. Walsh, M. I. Payne, P. Kumar, D. Liu, T. M. Pollock, M. D. Asta, R. O. Ritchie *et al.*, *Acta Mater.* **241**, 118380 (2022).
- [26] P. A. Santos-Florez, S.-C. Dai, Y. Yao, H. Yanxon, L. Li, Y.-J. Wang, Q. Zhu, and X.-x. Yu, *Acta Mater.* **255**, 119041 (2023).
- [27] J. Fisher, *Acta Metall.* **2**, 9 (1954).
- [28] E. Antillon, C. Woodward, S. Rao, and B. Akdim, *Acta Mater.* **215**, 117012 (2021).
- [29] S. Plimpton, *J. Comput. Phys.* **117**, 1 (1995).
- [30] X.-G. Li, C. Chen, H. Zheng, Y. Zuo, and S. P. Ong, *npj Comput. Mater.* **6**, 70 (2020).
- [31] Y. Zuo, C. Chen, X. Li, Z. Deng, Y. Chen, J. Behler, G. Csányi, A. V. Shapeev, A. P. Thompson, M. A. Wood *et al.*, *J. Phys. Chem. A* **124**, 731 (2020).
- [32] See Supplemental Material at <http://link.aps.org/supplemental/10.1103/PhysRevMaterials.8.013608> for further discussion and details associated with the methodology.
- [33] F. Körmann and M. H. Sluiter, *Entropy* **18**, 403 (2016).
- [34] V. Vitek, R. Perrin, and D. Bowen, *Philos. Mag.* **21**, 1049 (1970).
- [35] J. R. K. Bigger, D. A. McInnes, A. P. Sutton, M. C. Payne, I. Stich, R. D. King-Smith, D. M. Bird, and L. J. Clarke, *Phys. Rev. Lett.* **69**, 2224 (1992).
- [36] L. Ventelon and F. Willaime, *J. Comput.-Aided Mater. Des.* **14**, 85 (2007).
- [37] E. Clouet, *Phys. Rev. B* **84**, 224111 (2011).
- [38] J. Cowley, *Phys. Rev.* **138**, A1384 (1965).
- [39] N. Norman and B. Warren, *J. Appl. Phys.* **22**, 483 (1951).

- [40] F. Körmann, A. V. Ruban, and M. H. Sluiter, *Mater. Res. Lett.* **5**, 35 (2017).
- [41] P. Singh, A. V. Smirnov, and D. D. Johnson, *Phys. Rev. Mater.* **2**, 055004 (2018).
- [42] M. Widom, W. P. Huhn, S. Maiti, and W. Steurer, *Metallurg. Mater. Transact. A* **45**, 196 (2014).
- [43] H. Cook, *J. Phys. Chem. Solids* **30**, 2427 (1969).
- [44] B. S. Wyatt and B. Argent, *J. Less-Common Met.* **11**, 259 (1966).
- [45] A. Romig Jr. and M. Cieslak, *J. Appl. Phys.* **58**, 3425 (1985).
- [46] A. Abu-Odeh and M. Asta, *Acta Mater.* **226**, 117615 (2022).
- [47] X. Zhou, S. He, and J. Marian, *Materials* **15**, 5468 (2022).
- [48] A. Ferrari, Y. Lysogorskiy, and R. Drautz, *Phys. Rev. Mater.* **5**, 063606 (2021).
- [49] A. Melnick and V. Soolshenko, *J. Alloys Compd.* **694**, 223 (2017).
- [50] W. Chen, A. Hilhorst, G. Bokas, S. Gorsse, P. J. Jacques, and G. Hautier, *Nat. Commun.* **14**, 2856 (2023).
- [51] O. N. Senkov, G. Wilks, J. Scott, and D. B. Miracle, *Intermetallics* **19**, 698 (2011).
- [52] Y. Zou, S. Maiti, W. Steurer, and R. Spolenak, *Acta Mater.* **65**, 85 (2014).